Indentation Investigation of 304L Stainless Steel Friction Stir Weld Simulated Crack Repair

Nicolene van Rooyen[a], Madhumanti Bhattacharyya[b,c], Indrajit Charit[c,d], Michael R. Maughan[a1]

[a] Department of Mechanical Engineering, University of Idaho, 875 Perimeter Dr MS0902, Moscow, Idaho 83844, USA

[b] Department of Fuel, Minerals, and Metallurgical Engineering, IIT(ISM) Dhanbad, Dhanbad, Jharkhand 826004, India

[c] Department of Nuclear Engineering and Industrial Management, University of Idaho, Idaho Falls, ID 83402, USA

[d] Center for Advanced Energy Studies, University of Idaho, Idaho Falls, Idaho 83401, USA

[1] Corresponding author, maughan@uidaho.edu

Keywords:

Friction Stir Welding, Nanoindentation, Vickers Hardness, Crystallographic Texturing, Stainless Steel,

Abstract

Simulated cracks were repaired in 304L stainless steel using low temperature friction stir welding. Indentation studies were carried out to understand the effect of microstructural features on the mechanical property variation across the weld and to measure the size of the weld zones with a quantitative technique. Microhardness and nanoindentation hardness profiles were constructed on a transverse section across the weld. The data obtained were correlated by extrapolating the nanoindentation hardness to greater depths which showed that the nanoindentation hardness closely reflects the microhardness values throughout the weld. Grain size in the stir zone (SZ) was found to vary with the tool temperature which, in turn, alters the nanoindentation modulus variability and higher tool temperature resulted in widening of the SZ.

1. Introduction

Friction stir welding (FSW) is a versatile technique used for crack repair and solid-state joining of a variety of metallic systems, both similar and dissimilar [1]–[5]. The FSW process, by severe plastic deformation of the material and frictional heat generation, produces unique microstructural features and crystallographic textures. Like other welding processes, FSW leaves the material with several zones each possessing different microstructure and properties due to their processing history. These zones can have relatively distinct boundaries or diffuse interfaces depending on the material behavior and processing parameters [5].

As illustrated in Figure 1.a., a non-consumable high speed rotating tool, (Figure 1.b), is inserted and then moved along the faying surfaces or crack [1], [2], [5] in order to form the welded joint. Frictional heat generated due to the tool rotation increases the temperature locally resulting in the plastic flow of the material [5]. The rotation coupled with translation causes the material to plastically deform and flow around the tool, joining the material behind it [2]. This severe plastic deformation and frictional heat changes the microstructure of the base material (BM) in and around the weld, forming three distinct zones as shown in Figure 1.a. Each zone has its own thermo-mechanical history. The central stir zone (SZ) is enclosed by a thermomechanically affected zone (TMAZ), which is followed by a heat affected zone (HAZ) and then unaffected BM [1], [5]. These zones are further classified as advancing or retreating depending on their position relative to the rotation of the tool with respect to its traverse direction. From microstructural investigations it has been observed that the retreating HAZ (HAZ_R) to SZ transition is usually more diffused due to the complex material flow around the tool pin [6]. Material flow line features can be found within the SZ and are highly dependent on the processing parameters. One of these features is a set of metallurgical bands, commonly known as "onion rings," which manifest as a repeating pattern of second phase particle distribution, and/or grain orientation extending from where the tool contacts the material[5], [7], [8]. The joining line or "lazy-S" is the other material flow feature. It extends from the top surface to the bottom of the SZ [8]–[11]. The lazy-S region can have weak material bonding that adversely effects the mechanical performance of the weld [9]–[11].

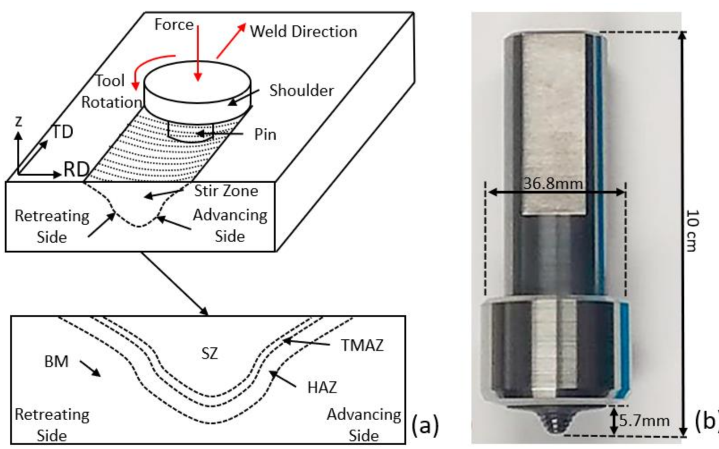

Figure 1 - (a) Friction stir welding process and microstructural zone illustration, (b) polycrystalline cubic boron nitride tool used for repair welding.

Intense shearing and resulting dynamic recrystallization develops a distinct crystallographic texture along the weld seam [1], [5], [12]. The texture evolution is heavily influenced by the travel and tool speeds [12]. The degree of crystallographic misalignment is decreased with increasing tool speed, which creates a more uniform crystallographic orientation within the SZ [12], [13]. Traditionally, electron backscatter diffraction (EBSD) is used to evaluate the texture of FSWed parts. However, this method is costly, requires specialized equipment, and careful preparation to obtain good results [1], [2]. Jeon et al. [14] used high resolution EBSD to study the microstructural development of FSWed single-crystal austenitic stainless steel. They concluded that simple shear deformation refined the SZ into a fine-grained polycrystalline aggregate [14]. Continuous and discontinuous recrystallization resulted in a final texture dominated by the ideal simple shear orientation [14].

Indentation methods have been used in tandem with EBSD to understand the process-microstructure-property relationship for FSWed parts. Microhardness is the most common indentation method used to assess the variations in mechanical properties across the SZ. Both microhardness profiles and contour maps have been correlated with EBSD imaging to evaluate the hardness distribution across all zones [15]–[18]; however, the diffuse transition from HAZ_R to SZ has not been consistently documented within hardness profiles and contour maps. This deficiency in the reporting of the diffuse transition from HAZ_R to SZ indicates that microhardness cannot give adequate resolution to assess microstructural changes over finer scale across the different zones.

Nanoindentation is a suitable alternative to microhardness and provides higher resolution due to its smaller length scale. The Meyer (nanoindentation) hardness and elastic modulus of the probed material are found from the nanoindentation data [19]. Meyer hardness differs from Vickers hardness by utilizing the projected area of contact instead of the actual surface area of contact. The elastic modulus is usually determined by analyzing the unloading slope obtained from the load vs. indentation depth data [19]. Comparing hardness measurements across length scales is complicated by the existence of the indentation size effect, which is an increase in hardness with decreasing indentation size [20]–[23]. The increased hardness is believed to result from geometrically necessary dislocations formed by inherently large strain gradients present in small indentations [22] and from other defect structures [24]. The theoretical infinite depth hardness found from the Nix-Gao model [22] represents an extrapolation of the hardness to depths where geometrically necessary dislocations have negligible effect on hardness and can be used to connect nanoindentation data to the microhardness length scale.

The elastic modulus information gained from nanoindentation has been used to understand the influence of grain orientation (crystallographic texture) on mechanical properties of polycrystalline materials [25]–[27]. It is well known that mechanical properties differ among grains of different orientations [28], [29]. Most anisotropic property investigations by nanoindentation were done on samples where the average grain size is sufficiently larger than the indent plastic zone. This ensures that the obtained elastic modulus matches the specific crystallographic orientation of the grain and is usually validated by EBSD [25], [26]. It is important to note that the elastic modulus is documented to be relatively constant with position when the indentation impression is equal to or larger than the average grain size [27]. Variation in the elastic modulus of materials with small grains with a predominant texture has not been explored.

Nanoindentation has been used to characterize FSWed aluminum alloys; however, similar studies on FSWed steel are sparse. In steels, nanoindentation has been used to probe the effect of specific phases on localized hardness as well as the microstructure-hardness evolution across the SZ [30]–[32]. However, the nanoindentation hardness profiles, across the FSW region, reported by Legendre et al. [31] and Chaudry et al. [32] were only partial in nature and did not attempt to distinguish the property transition from SZ to TMAZ to HAZ when correlated to the microstructure. Very fine spatial variations in hardness and elastic modulus information provided by nanoindentation has given valuable knowledge about microstructure-property relationships and residual stress [4], [28], [33], [34]. It has been shown that the elastic modulus of aluminum alloy changes within each zone [33], [34]. However, the influence of average grain size and dominant texture on the mechanical properties within each zone have not been investigated. Understanding these relationships could lead to advances in FSW technology, enabling tailored weld properties or improvements in weld placement based on knowledge of material performance.

This work builds on previous investigations of processing-microstructure-property relationships in FSW [3]. Microhardness and nanoindentation will be used to characterize mechanical property variations across two FSW in 304L stainless steel (SS) samples prepared with different processing parameters. Detailed indentation studies of properties on a 725 °C welded sample were conducted to characterize FSW zones, nanoindentation modulus variations, and microstructural features. An 825 °C welded specimen was also investigated to understand the processing influence on mechanical properties.

2. Methods

Two sets of FSW process parameters were used to repair simulated cracks in 304L SS plates. Samples machined from a section transverse to the welding direction were used for microscopy, indentation, and uniaxial tensile tests. Three indentation investigations were conducted. First Vickers hardness testing was used to construct microhardness profiles across the weld zones. Next nanoindentation was used to construct similar profiles, except these profiles collected Meyer hardness and elastic modulus. Lastly, nanoindentation was also used to characterize the indentation size effect of the SZ, TMAZ, and HAZ at discrete locations. The indentation investigations were conducted close to the top surface and base of the weld Figure 2.a).

2.1. FSW Sample Preparation & Microscopy

Electric discharge machining was used to introduce simulated cracks (0.33 mm wide and 5 mm deep) in the center, along the length of a 330 mm ×149 mm ×12.7 mm 304L SS plates. The chemistry of the hot rolled and annealed 304L SS plates was supplied by Rolled Alloys, Inc. and is provided in Table 1. The tool shown in Figure 1.b along with two sets of welding parameters were used to repair the simulated cracks. The temperatures were selected experimentally to give an idea of different behaviors within the range of workable parameters without introducing weld defects. In the first case, the weld repair was done at 725°C with a tool rpm of 63-69 rev/min and a vertical axial load of 48.8 kN. The second sample was repaired at 825°C using a tool speed of 95-130 rev/min and a vertical axial load of 51.1 kN. In both the cases, a constant travel speed of 25.4 mm/min was maintained and the load was determined by the control algorithm of the FSW machine. Other details of the welding process are outlined in the work by Bhattacharyya et al. [3].

Table 1 - Supplier provided chemistry for the as-received 304L SS plate

Element	**C**	**Mn**	**P**	**S**	**Si**	**Cr**	**Ni**	**Mo**	**Cu**	**N**	**Nb**	**Ti**
Wt. %	0.016	1.53	0.06	<0.001	0.32	18.34	8.17	0.32	0.43	0.09	0.021	0.003

The sample for microscopy was prepared by grinding with silicon carbide paper starting at 600 grit and successively working down to 1200 grit. The sample was electrochemically etched after it was polished with 3 µm and 1 µm diamond suspension. Etching was achieved by submerging the sample surface in a 10% oxalic acid solution with 10 V applied for 10 s. Figure 2.a shows the electrochemically etched sample. An AmScope ME520TA optical microscope was used for microstructural investigation. Average grain size was determined using the mean linear intercept method [35]. The sample was repolished using the same procedure prior to the indentation testing. After nanoindentation, the sample was again electrochemically etched to obtain better contrast during higher magnification imaging of the indentations using a Zeiss Supra 35VP field emission gun scanning electron microscope (SEM). These secondary electron (SE) SEM images were captured with a working distance of 10 mm and acceleration voltage of 5 kV.

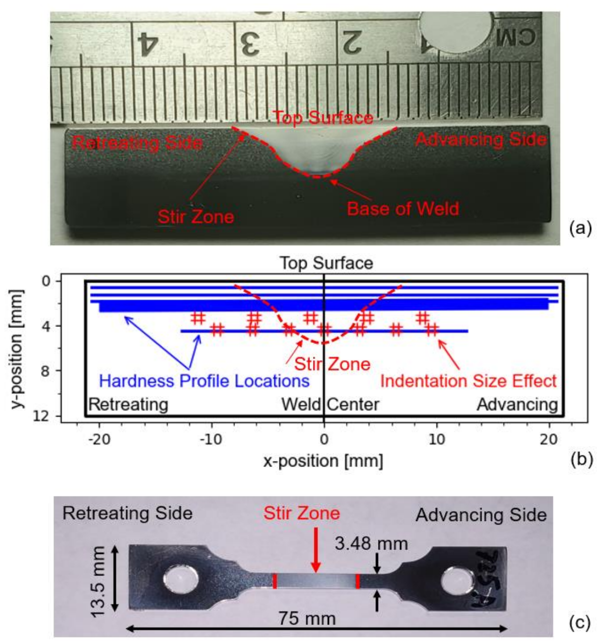

Figure 2 - (a) FSW sample with indicated stir zone, advancing side and retreating side. (b) Hardness versus depth, microhardness, and nanoindentation locations, and (c) uniaxial tensile test specimen orientation relative to weld direction.

2.2. Indentation Methods

Microhardness tests were conducted using a LECO LM-100 Vickers microhardness tester under 200 g-f load. The microhardness tests consisted of three "lines" of indents across the weld. Figure 2.b shows each microhardness line was spaced 0.635 mm from the next. Table 2 shows the distances from the top surface of the sample and the acronyms for various indentation profiles. The values in line VH1 through VH3 were previously presented in [3]. Each microhardness line consisted of 60 indents spaced 0.635 mm apart.

Table 2 - Hardness mapping line locations relative to top surface of the sample and associated acronyms

Indentation Method	Acronym	Distance from Top [mm]
725 °C Microhardness Line 1	VH1	0.635
725 °C Microhardness Line 2	VH2	1.270
725 °C Microhardness Line 3	VH3	1.905
725 °C Microhardness Line 4	725-VH7	4.445
725 °C Nanoindentation Line 1	N1	1.867
725 °C Nanoindentation Line 2	N2	2.067
725 °C Nanoindentation Line 3	N3	2.280
725 °C Nanoindentation Line 4	N4	2.480
725 °C Nanoindentation Line 5	N5	2.680
725 °C Nanoindentation Line 6	725-N4	4.345
825 °C Microhardness Line 1	825-VH7	4.445
825 °C Nanoindentation Line 4	825-N4	4.496

The nanoindentation tests were conducted with a KLA G200 Nanoindenter (Milpitas, CA) equipped with a diamond Berkovich tip. Five lines of 220 nanoindentations were constructed close to the top surface for the 725 °C sample only. Along with a total of 128 nanoindentations, for both 725 °C and 825 °C samples, were constructed close to the base of the weld (Figure 2.a). The nanoindentation lines were created at the locations indicated by "hardness profile locations" in Figure 2.b. For these indents, the sample was loaded linearly to 20 gf (196.1 mN) within 15 s and held constant for 30 s before linear unloading in 10 s. The maximum indentation depth varied from 1450 nm to 1875 nm. The thermal drift for all nanoindentation tests was below 0.1 nm/s and all indent data were corrected with the individually recoded drift rate. Indents were spaced 200 µm apart which is approximately 10 times the indentation "diameter" to avoid testing the plastically deformed region created by the previous indent [36]. Standard nanoindentation data processing was conducted to determine indentation hardness and sample modulus with an assumed

Poisson's ratio of 0.07 for the indenter and 0.29 for the sample [19]. The nanoindentation hardness was converted to Vickers hardness using Equation 1 [37].

$$VH = 0.094495 \times H \quad (1)$$

In Equation 1, *VH* refers to the microhardness and reflects the relationship between the applied load and the actual surface area of the impression. Whereas the nanoindentation hardness, H, is a measure of the mean contact pressure using the projected contact area of the indenter tip. To minimize the grain boundary effect [25], [38] a custom Python script was used to discard the datapoints which deviated more than 8% from the average nanoindentation hardness of a simple moving average (moving with position across the specimen) [33]. In this case, the average at each position was calculated from a total of 10 indents, five forward-looking and five backward-looking compared to the current indent. After removing the outliers, the data were smoothed using a Fast Fourier Transform filter to obtain a continuous profile from the large number of indents.

2.3. Indentation Size Effect Characterization

Hardness vs. depth data were captured at each of five locations indicated by the '*#*' symbol in Figure 2.b to characterize the indentation size effect of the different regions comprising the FSWed samples [21] and facilitate comparisons between nanoindents and microhardness indents despite their size. The sample was cyclically loaded to a maximum load of 85 gf (833.85 mN). A total of five cycles, evenly spaced between 0 gf and 85 gf (833.85 mN), were completed for each indent, with 500 µm spacing between each indent. Each cycle was linearly loaded within 15 seconds and held constant for 30 seconds and unloaded within 10 seconds. Four indentations were conducted at each location. The data were fit to Equation 2 [22] to determine the hardness at deep depths in the SZ, TMAZ, and HAZ.

$$H(H_0, h) = H_0\sqrt{1 + \frac{h^*}{h}} \quad (2)$$

In Equation 2, H is the nanoindentation hardness, h is the indentation contact depth, h^* is a fitting parameter, and H_0, is the infinite depth hardness, which is assumed to reasonably represent the microhardness. Once H_0 was determined for each location, the value was also converted to microhardness using Equation 1.

2.4. Uniaxial Tensile Tests

Three tensile samples (Figure 2.c) from each temperature were prepared such that the stir zone was within the gauge length (25.4 mm). The thickness and width of the samples were 1.38 mm and 3.48 mm, respectively. Uniaxial tensile tests were conducted at room temperature with a strain rate of 10^{-3} s^{-1} using an Instron 5982 universal tester.

3. Results

3.1. Microstructure Analysis

Figure 3 shows a composite micrograph of the 725 °C FSWed sample from a transverse section. The BM microstructure had recrystallized equiaxed grains with an average grain size of 47±16 µm. The SZ had a basin shape that was widest at the top surface, followed by a sharp decrease in width towards the center, and a gradual decrease in width until the bottom of the weld nugget. The base of the weld nugget was approximately 5.5 mm from the top surface. As expected, the SZ was enclosed by the TMAZ and then the HAZ on either side. In Figure 3 the transition between the different zones appears more diffused on the retreating side of the weld. The microstructure changed from small equiaxed grains, with average grain size 2.3±0.3 µm within the SZ, to severely deformed elongated grains in the TMAZ. The same observations are present in the 825 °C sample shown in Figure 4, except for a wider SZ and larger SZ average grain size of 4.6±0.6 µm, compared to the 725 °C sample.

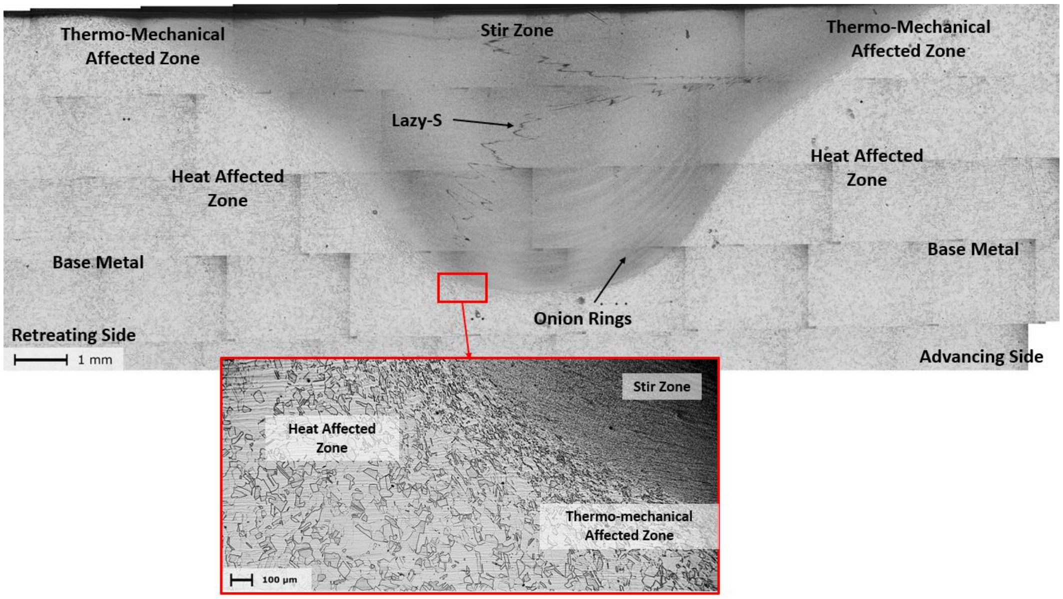

Figure 3 - Composite micrograph of various zones in 304L SS FSW sample prepared with 725 °C tool temperature.

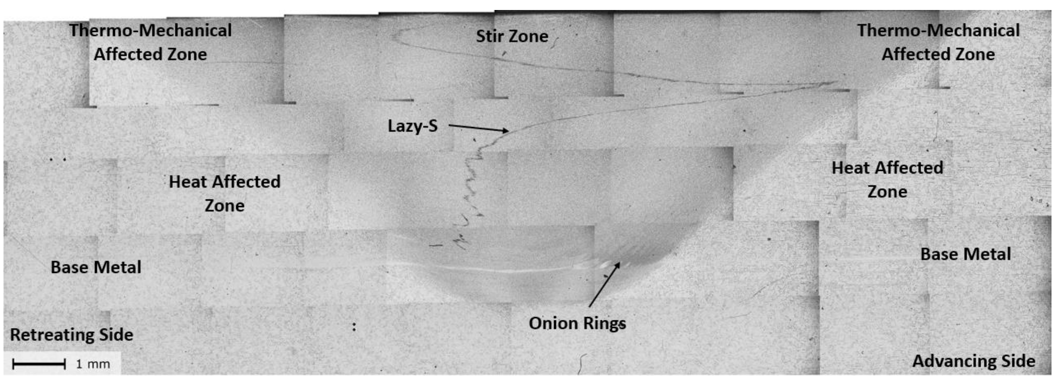

Figure 4 - Composite micrograph of various zones in 304L SS FSW sample prepared with 825 °C tool temperature.

Onion rings and the ‘lazy-S’ were the two material-flow-induced features found within the SZ of both samples (Figure 3 and Figure 4). The onion rings appear under microscope as light-colored bands that reflect the basin shape of the SZ. These flow lines were only present in the advancing side of the SZ, stretching from ~1 mm from the top surface to the base of the weld nugget. The onion ring spacing decreased from the center of the SZ toward the TMAZ. Fewer onion rings were present in the 825 °C sample compared to the 725 °C sample. The ‘lazy-S’ was a nonuniform spiral feature that stretched from the top surface to roughly 0.4 mm from the base of the weld nugget.

3.2. Microhardness and Nanoindentation Hardness Profile Comparison

Figure 5.a shows the nanoindentation hardness vs. indent depth of four indents within the 725 °C SZ, close to the weld center. The hardness decreased from 320 HV to 280 HV over a depth range of 2 μm within the SZ, typical of the indentation size effect. The initial hardness decrease was similar for the TMAZ and HAZ, but the overall profiles were shifted slightly downward (softer). The H_0 values for all regions determined were then plotted with the nanoindentation and microhardness profiles as shown in Figure 5.b. This plot shows the hardness across the entire weld section starting from the BM on the retreating side and ending in the BM on the advancing side of the 725 °C sample. The nanoindentation hardness profiles were shifted upward (harder) on the plot due to the indentation size effect. It is evident from Table 3that the Nix-Gao fitting parameters are unique for each zone. H_0 was highest within the SZ then successively lowers moving outward from the weld center. The H_0 profile closely matches the VH3 microhardness profile. There is one exception that is on the cusp between the SZ and TMAZ on the advancing side where H_0 is lower by 41 HV compared to the microhardness value at that location.

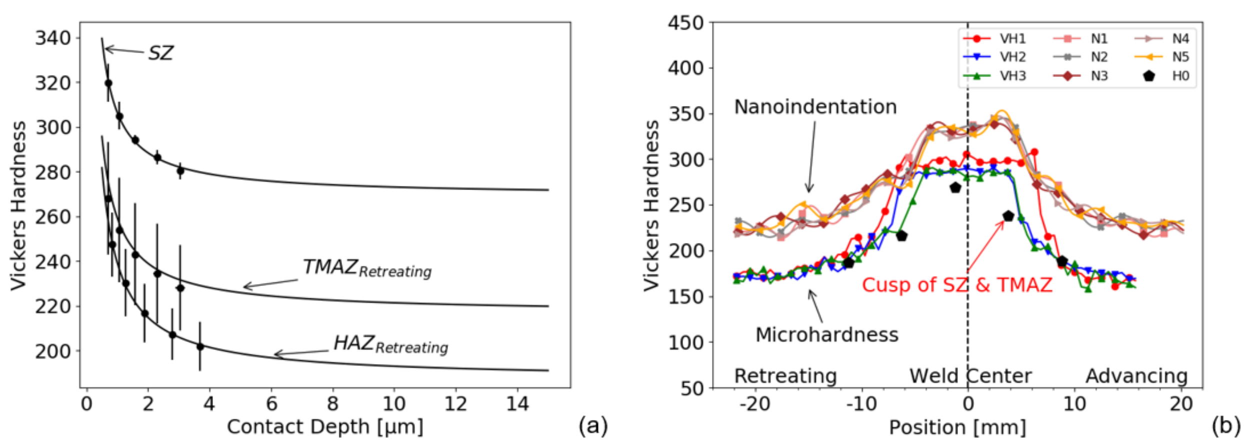

Figure 5 -(a) Nix-Gao fit of cyclical nanoindentation indents in the SZ. (b) Microhardness and nanoindentation hardness profiles across the 725 °C 304L SS FSW sample, and infinite depth hardness (H0).

The VH3 and N1 profiles (Figure 6) were chosen to compare methods for determining the widths of the TMAZ and HAZ due to their proximity to one another. The width of each region was calculated by evaluating the slope changes across each hardness profile. Plotting the linear slope between two consecutive hardness values vs. position produced a varying profile, where significant changes in slope or inflection points indicate the transition points between different zones. The different zone widths calculated for VH3 and N1 are presented in Table 3.

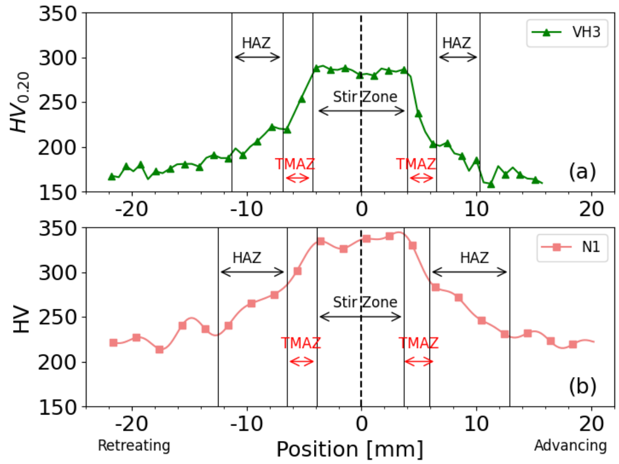

Figure 6 - (a) Microhardness profile 1.905 mm from the top surface, (b) nanoindentation hardness profile 1.867 mm from the top surface of the 725 °C sample.

Table 3 - Infinite depth microhardness, microhardness widths, and nanoindentation widths of each zone of the 725 °C approximately 1.905 mm from the top surface.

	HAZ$_R$	**TMAZ$_R$**	**SZ**	**TMAZ$_A$**	**HAZ$_A$**
VH3 [mm]	4.4	2.5	8.3	2.5	3.8
N1 [mm]	6.0	2.6	7.6	2.2	7.0
H_0 [HV]	187.08	216.64	269.07	237.76	188.10
h* [nm]	633.36	431.46	296.03	322.65	662.80

Figure 7 compares the infinite depth hardness along with microhardness and nanoindentation profiles of both 725 °C and 825 °C FSWed samples close to the base of the weld. The 825 °C hardness profiles were softer compared with the 725 °C profile. From Table 4 it is evident that higher tool temperature resulted in a wider SZ and narrower TMAZ and HAZ, on both the retreating and advancing side. The 725 °C H_0 values closer to the base of the weld are slightly higher than those closer to the top surface.

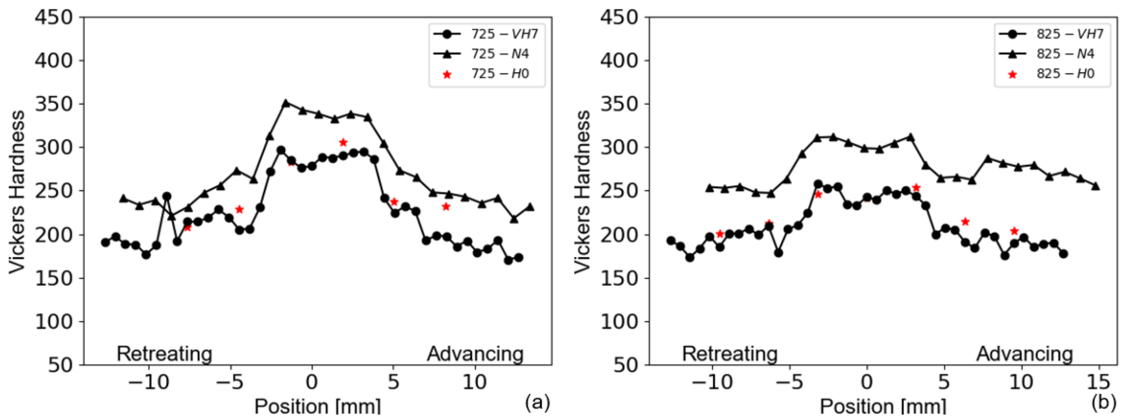

Figure 7 - Microhardness and Nanoindentation profiles approximately 4.445mm from the top surface for (a) 725 °C and (b) 825 °C FSWed sample.

Table 4 - Infinite depth microhardness, microhardness widths, and nanoindentation widths of each zone of the 725 °C and 825 °C samples at approximately 4.445 mm from the top surface.

	725 °C				**825 °C**			
	Vickers Width [mm]	Nanoindentation Width [mm]	H_0 [HV]	h* [nm]	Vickers Width [mm]	Nanoindentation Width [mm]	H_0 [HV]	h* [nm]
HAZ_R	3.8	5.2	228.5	403.2	2.2	2.3	215.2	491.5
$TMAZ_R$	2.2	2	283.1	166.1	1.8	1.3	253.4	279.6
SZ	5.4	5.2	305.2	146.8	6.1	5.9	241.5	244.6
$TMAZ_A$	1.6	1.6	237.4	130.3	0.9	1.1	246.6	246.0
HAZ_A	4.6	4.8	237.41	342.19	2.9	2.7	212.2	411.51

3.3. Uniaxial Tensile Test – Nanoindentation Comparison of Elastic Modulus

Figure 8 shows the elastic modulus profile generated by nanoindentation for line N1 (725 °C sample). In this plot the coefficient of variance (COV) of the elastic modulus is indicated with the black bars. The COV was calculated by determining the standard deviation of each point, then dividing it by the mean of the moving-average window. The length of the bars indicates that the variability of the elastic modulus is much lower in the SZ compared to other regions. A cluster of consecutive indents that measure the same elastic modulus is present in the base metal. Figure 8 also shows that the uniaxial tensile test elastic modulus is slightly lower than the average indentation modulus across all zones. The tensile test and nanoindentation elastic moduli for the 725 °C sample are 201 GPa and 214 GPa, respectively.

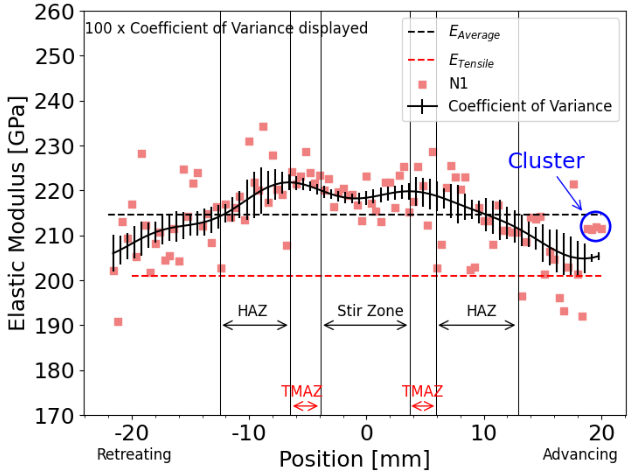

Figure 8 - Nanoindentation elastic modulus profile of the 725 °C sample 1.867mm from the top surface.

The tensile test results for BM and FSWed samples are outlined in Table 5 and the corresponding engineering stress-strain curves along with post-fracture images of the tensile samples are shown in Figure 9.a and Figure 9.b, respectively. The most notable differences between the as-received BM and the FSWed samples are with respect to the yield strength (YS), uniform elongation, and elongation to fracture. The YS of the FSWed samples is ~116 MPa higher than the as-received BM. Whereas both the uniform elongation and elongation to fracture are less than half of the as-received BM. The 825 °C specimen had slightly higher yield and ultimate tensile strengths compared to the 725 °C. As shown in Figure 9.b, both the 725 °C and 825 °C samples fractured within the BM well outside the SZ.

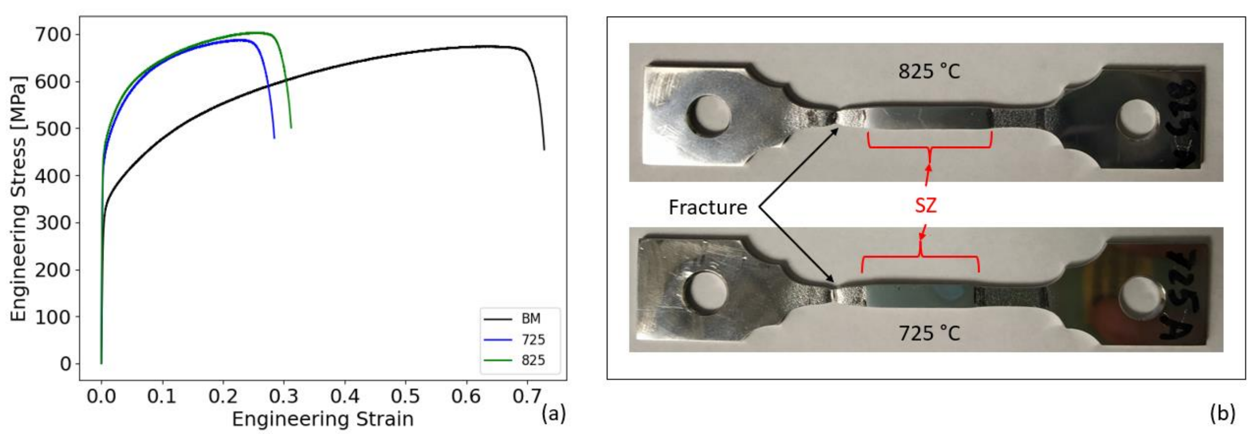

Figure 9 - (a) Engineering stress-strain curve of 725 °C, 825 °C, and BM. (b) 725 °C and 825 °C tensile samples post-fracture.

Table 5 - Tensile properties of the BM and FSW 304L SS (± indicate one standard deviation)

Sample	Elastic Modulus [GPa]	Yield Strength [MPa]	Ultimate Tensile Strength [MPa]	Uniform Elongation [%]	Elongation to Fracture [%]
BM	196±1.5	312±2.0	678±7.0	62.5±1.0	70.3±2.0
725 °C FSW	201±4.2	428±6.0	690±3.5	22.8±0.1	28.3±0.1
825 °C FSW	202±2.8	444±5.0	698±7.0	25.6±0.2	30.5±0.7

4. Discussion

4.1. Microstructural Characterization

The fine equiaxed grains within the SZ result mostly from dynamic recrystallization [17], [39]. The distinct basin shape of the SZ is caused by severe plastic deformation and frictional heating between the material and the tool profile [2]. EBSD analyses, at discrete locations within the SZ, indicate high fraction of low angle grain boundaries [3]. This coupled with nominal grain size differences at the probed locations suggest that only partial recrystallization occurred resulting in the formation of substructures within the SZ and is attributed to the temperatures resulting from the FSW processing parameters [3]. Differences in material flow on the advancing and retreating side for the rotating tool affect the transition sharpness from the SZ to HAZ seen in Figure 3 and Figure 4 [39], [40]. Increased mixing on the retreating side promotes a wider and more diffuse transition between the two different zones [6]. Mixing is promoted on the retreating side because the weld travel speed and tool rotation are in opposite directions [6]. These differences in material flow on the advancing and retreating side for the rotating tool affect the transition sharpness from the SZ to HAZ seen in Figure 3 and Figure 4. Presence of elongated grains within the TMAZ can be attributed to insufficient plastic strain and smaller heat input in the TMAZ as compared to the SZ. Unlike HAZ, the material in TMAZ undergoes thermal cycle as well as small amount of plastic deformation causing the elongation of the grains. However, the smaller strain in TMAZ doesn’t provide sufficient driving force for complete recrystallization to happen. Also, the extent of the deformation induced heat is small in TMAZ as compared to that in the SZ. This results in dynamically recovered elongated grains with substructures in the TMAZ [2].

The onion rings reflect localized differences in grain size and particulate density within the SZ. These localized differences are caused by deformation differences resulting from shear layer flow [2], [6], [41]. The 'lazy-S' appears because of impaired mixing, promoted by the presence of second phase particles, along the vortex of the material flow [3], [9]. As reported by Bhattacharyya et al., SEM-EDS analysis of this sample showed indications of second phase particles within the onion rings and the 'lazy-S' [3].

4.2. Comparison of Indentation Methods

The indentation size effect was characterized for different regions of the 725 °C sample to validate that nanoindentation hardness can be correlated with microhardness values. This characterization showed that each zone has a unique indentation size effect. The average grain size is smallest within the SZ then successively grows outward from the weld center. The H_0 profile in Figure 5.b. closely reflects that of VH3, except for one outlier at the cusp between the SZ and TMAZ. At this location three of the four indents were within the TMAZ with one in the SZ which inflates H_0 at this point. The consistency of H_0 with the microhardness profile VH3 indicates that nanoindentation can be quantitatively compared with Vickers when the appropriate data corrections are used.

The bell-shaped nanoindentation hardness and microhardness profiles in Figure 5.b results from the heterogeneous microstructure due to likely partial recrystallization, differences in particulate density, and presence of second phase particles within in the SZ along with the process of grain refinement within the SZ, TMAZ, and HAZ [17]. The observed bell-shape is consistent with literature observations [16]–[18], [32]. The BM and SZ grain size relative to nanoindentation impression is shown in Figure 1010.a and Figure 1010.b, respectively. These profiles for FSWed steels are usually characterized by a diffuse increase in hardness from the retreating BM to a plateau within the SZ followed by a sharp decrease to the BM on the advancing side [2], [42].

The VH1 plateau is significantly wider than VH2 and VH3 (Figure 5.b). This is expected because VH1, VH2, and VH3 are successively further from the top surface of the sample. The nanoindentation profiles indicate no significant differences in the width of the plateau within the SZ and have a similar width to

VH3. This is because the nanoindentation profiles are spaced much closer together and over the same region that is represented by VH3.

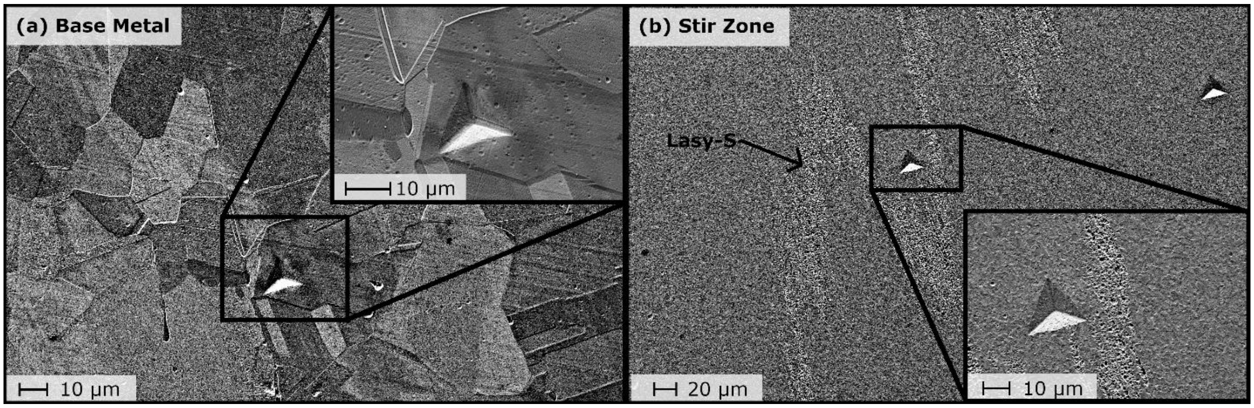

Figure 10 – SE SEM image of nanoindentation size relative to grain size in (a) base metal and (b) stir zone of the 725 °C sample.

The indentation method comparison of the 725 °C sample shown in Figure 6 indicates that nanoindentation was able to detect the slight differences between $TMAZ_R$ and $TMAZ_A$ widths, whereas microhardness testing does not. The TMAZ widths measured using microhardness testing were the same, 2.54 mm, on both the advancing and retreating side. Using nanoindentation, however, $TMAZ_R$ and $TMAZ_A$ were found to be 2.6 mm and 2.2 mm respectively. Nanoindentation also captured the slight microstructural changes within the HAZ by detecting small spatial changes in hardness. These changes correlate to the gradual grain size increase from the innermost zone within the HAZ (closest to TMAZ) to the outermost region (closest to BM). Given the data collected in this study grain size is likely to be the major contributor to hardness changes, but the presence of second phase particles, particularly around the lazy-S could play a role. In this case, the HAZ_R width measured using nanoindentation was 6.0 mm, which is 1.56 mm wider than the width determined by microhardness testing. The difference in width between nanoindentation and microhardness for HAZ_A is even larger. Here the nanoindentation-measured HAZ_A is 7 mm wide, 3.19 mm wider than the microhardness width. The nanoindentation method, due to its smaller length scale, is more sensitive to spatial microstructural changes within the HAZ and provides greater resolution compared to microhardness testing; thus, making nanoindentation more suitable for estimating the HAZ width of FSWed materials.

Difference in average grain size between the 725 °C and 825 °C samples indicates that more grain growth occurred in the 825 °C sample following recrystallization. This results in the downward shift of hardness profiles and lower H_0 values reported for the 825 °C sample (Figure 8 and Table 4). The widening of the SZ with increased tool temperature has been documented for 316L SS and is attributed to discontinuous dynamic recrystallization and grain growth within samples prepared with higher tool temperature [18].

The 725 °C hardness profiles and H_0 values closest to the top surface (Table 3), where the grains are larger, are shifted lower compared to those closest to the base of the weld (Table 4), where the grains are smaller. This shows that microhardness and nanoindentation can detect the heterogeneous grain size distribution within the SZ, which has been documented in previous work using EBSD [3].

4.3. Uniaxial Tensile Test – Nanoindentation Elastic Modulus Comparison

The increase in YS (

Table 5) of the FSWed samples are caused by the grain refinement within the SZ. Necking occurred in the transition region between the BM and the retreating HAZ and resulted in fracture within the BM for both 725 °C and 825 °C samples (Figure 9.b). Most of the elongation occurred outside the SZ and is attributed to the microstructural change observed from the center of the weld to the BM. EDS analysis, conducted during the precursory study, showed significant presence of delta ferrite stringers within the BM but scarce presence within the SZ [3]. The larger grain size and significant presence of these stringers within the BM could have influenced the flow behavior between the delta ferrite and austenite interfaces, promoting elongation outside the SZ. The widening of the 825 °C SZ likely resulted in the slight increase observed for YS and UTS [3]. The gauge region of the sample has zones with varying microstructure. This composite structure causes a strength mismatch, resulting in reduced ductility compared to the homogeneous as-received BM.[3].

The average elastic modulus determined by nanoindentation, for the 725 °C sample, is 15 GPa higher than uniaxial tensile tests (Figure 8). Comparing the physical sample size of the tensile test to that of nanoindentation, it is apparent that the amount of material tested by nanoindentation is less. The average indentation elastic modulus is biased by the number of indents within the SZ compared to the BM. If more indents were conducted in the BM, the average would shift lower, closer to that measure by the tensile tests. The gradual increase and then decrease in modulus from the retreating to advancing side of the weld indicates that crystallographic texture is also influencing the elastic modulus. The relationship between crystallographic texture and elastic modulus are discussed in detail in the next section.

4.4. Indentation Variability and Relationship to Crystallographic Texture

Face centered cubic (FCC) materials like austenitic steels exhibit highly anisotropic behavior with crystallographic orientation [29]. Evident from Figure 1010.b, the nanoindentation elastic modulus within the SZ reflects the average of many small equiaxed grains. Thus, assessing the elastic modulus COV in different regions of the FSWed sample should identify crystallographic texture changes.

In regions where grain size is larger than the indent size, increased variability will result. This is because individual indents will return only the modulus of that large grain. In regions where the grain size is much smaller than the indent size, the average modulus of many grains with unique orientations will be returned resulting in a low COV. Figure 1010.a. shows that the nanoindentation impressions are smaller than the grain size in the BM zone, where a single indentation is more likely to probe a specific crystallographic orientation rather than that of many grains. This is further substantiated by the clustering of elastic modulus values within the advancing BM, which would result from several indents in a single large grain (Figure 8). The COV within the SZ is significantly smaller than the other regions within the FSWed sample (Figure 8). This is due to the average grain size being significantly smaller than the nanoindentation impression in this zone [27]. The resulting elastic modulus within the SZ is thus representative of the average of many grains.

EBSD analysis using orientation distribution mapping and orientation distribution function in 304 stainless steel from Hajizadeh et al. [13] indicates a simple shear texture within the SZ, predominantly aligned in the <110> direction. The BM of Hajizadeh et al. was equiaxed and randomly oriented. Since the processing parameters were similar, it can be assumed that the dominant orientations in the weld zones of the present study are similar. Equation 3 can be used to determine the modulus in any crystallographic direction based on the modulus in the <100> and <111> directions [29].

$$\frac{1}{E_{[hkl]}} = \frac{1}{E_{<100>}} - 3\left(\frac{1}{E_{<100>}} - \frac{1}{E_{<111>}}\right)(\alpha^2\beta^2 + \alpha^2\gamma^2 + \beta^2\gamma^2) \quad (3)$$

In Equation 3, α, β, and γ represent the direction cosines of the crystallographic directions and E is the elastic modulus in the direction indicated by the subscript. For AISI 304L stainless steel $E_{<100>}$ and $E_{<111>}$ are 179 GPa and 208 GPa, respectively [26]. The elastic modulus within the SZ ($\sim E_{<110>}$) was calculated to be 200 GPa by substituting the values for $E_{<100>}$, $E_{<111>}$, and the direction cosines for the <110> direction into Equation 3. This is in reasonable agreement with measured indention values within the SZ, considering the variable nature of individual grain orientations within textures, slight off-axis character of the sample texture from the <110> direction, and hemispherical plastic zone sampled by the indenter [43]. The profile in Figure 6 shows the change in modulus across the weld, indicating that nanoindentation can be used to estimate changes of the dominant crystallographic texture within the metallurgical zones, once calibrated.

5. Conclusions

The indentation size effect was characterized for the SZ, TMAZ, and HAZ of FSWed 304L. H_0 determined from the indentation size effect was used to determine zone widths between nanoindentation and microhardness. Using nanoindentation the TMAZ width is slightly larger and the HAZ is significantly larger than that determined by microhardness. Elastic modulus profiles generated by nanoindentation showed increased variability within the BM compared to the SZ. From these observations the following conclusions can be drawn:

- A higher tool temperature results in widening of the SZ, increased grain growth, and reduced overall hardness.
- Changes in average grain size between each zone results in unique indentation size effects within each zone.
- H_0 values determined by nanoindentation closely reflect the microhardness values.
- Nanoindentation has adequate resolution to capture slight microstructural changes across the different zones.
- Variations of elastic modulus across the weld are due to texture.
- The significantly smaller average grain size within the SZ caused the elastic modulus COV in this zone to be substantially smaller than TMAZ, HAZ, and BM COV.

In the future, contour maps of both hardness and elastic modulus determined by nanoindentation area aimed to be generated for FSW parts and compared with EBSD to assess if nanoindentation can capture the dominant texture within the SZ. Creating contour maps will also determine if nanoindentation can capture material flow-induced features (onion rings and 'lazy-S').

Declaration of Competing Interests

All authors declare that they have no known competing financial interests or personal relationships that could have appeared to influence the work reported in this paper.

Acknowledgement

This work is partly supported by the US DOE Office of Nuclear Energy under award number DE-NE0008776. The authors wish to thank Dr. Saumyadeep Jana for providing the friction stir welded 304L SS Plate used in the present study.

Authorship Contribution Statement

Nicolene van Rooyen: Conceptualization, Writing – Original Draft, Writing – Review & Editing, Investigation, Methodology, Formal analysis, Visualization, Data Curation, Software. **Madhumanti Bhattacharyya**: Conceptualization, Writing – Writing – Review & Editing, Investigation, Data Curation. **Indrajit Charit**: Supervision, Funding Acquisition, Writing – Review & Editing. **Michael R. Maughan**: Conceptualization, Supervision, Resources, Formal analysis, Writing – Original Draft, Writing – Review & Editing

References

[1] A. J. Schwartz, M. Kumar, B. L. Adams, and D. P. Field, Eds., *Electron Backscatter Diffraction in Materials Science*. Boston, MA: Springer US, 2009. doi: 10.1007/978-0-387-88136-2.

[2] R. S. Mishra and Z. Y. Ma, "Friction stir welding and processing," *Mater. Sci. Eng. R Rep.*, vol. 50, no. 1, pp. 1–78, Aug. 2005, doi: 10.1016/j.mser.2005.07.001.

[3] M. Bhattacharyya, A. Kundu, K. S. Raja, J. Darsell, S. Jana, and I. Charit, "Processing-microstructure-property correlations for temperature-controlled friction stir welding of 304L SS plates," *Mater. Sci. Eng. A*, vol. 804, p. 140635, Feb. 2021, doi: 10.1016/j.msea.2020.140635.

[4] G. Peng *et al.*, "Nanoindentation Hardness Distribution and Strain Field and Fracture Evolution in Dissimilar Friction Stir-Welded AA 6061-AA 5A06 Aluminum Alloy Joints," *Adv. Mater. Sci. Eng.*, vol. 2018, pp. 1–11, Oct. 2018, doi: 10.1155/2018/4873571.

[5] R. S. Mishra, P. S. De, and N. Kumar, *Friction Stir Welding and Processing: Science and Engineering*, 1st ed. 2014. Cham: Springer International Publishing : Imprint: Springer, 2014. doi: 10.1007/978-3-319-07043-8.

[6] A. Polar, F. Rumiche, M. Pareek, and J. E. Indacochea, "Friction stir welding of copper: metallurgical characterization and corrosion resistance.," in *Trends in Welding Research: Proceedings of the 7th anual International Conference*, 2005, pp. 431–436.

[7] Z. W. Chen and S. Cui, "On the forming mechanism of banded structures in aluminium alloy friction stir welds," *Scr. Mater.*, vol. 58, no. 5, pp. 417–420, Mar. 2008, doi: 10.1016/j.scriptamat.2007.10.026.

[8] S. Xu, "A study of texture patterns in friction stir welds," *Acta Mater.*, vol. 56, no. 6, pp. 1326–1341, Apr. 2008, doi: 10.1016/j.actamat.2007.11.016.

[9] T. Le Jolu *et al.*, "Microstructural Characterization of Internal Welding Defects and Their Effect on the Tensile Behavior of FSW Joints of AA2198 Al-Cu-Li Alloy," *Metall. Mater. Trans. A*, vol. 45, no. 12, pp. 5531–5544, Nov. 2014, doi: 10.1007/s11661-014-2537-1.

[10] Y. S. Sato, H. Takauchi, S. H. C. Park, and H. Kokawa, "Characteristics of the kissing-bond in friction stir welded Al alloy 1050," *Mater. Sci. Eng. A*, vol. 405, no. 1–2, pp. 333–338, Sep. 2005, doi: 10.1016/j.msea.2005.06.008.

[11] H.-B. Chen, K. Yan, T. Lin, S.-B. Chen, C.-Y. Jiang, and Y. Zhao, "The investigation of typical welding defects for 5456 aluminum alloy friction stir welds," *Mater. Sci. Eng. A*, vol. 433, no. 1–2, pp. 64–69, Oct. 2006, doi: 10.1016/j.msea.2006.06.056.

[12] J.-H. Cho and P. R. Dawson, "Investigation on Texture Evolution during Friction Stir Welding of Stainless Steels," *Metall. Mater. Trans. A*, vol. 37A, pp. 1147–1164, 2006.

[13] M. Hajizadeh, S. Emami, and T. Saeid, "Influence of welding speed on microstructure formation in friction-stir-welded 304 austenitic stainless steels," *Int. J. Miner. Metall. Mater.*, vol. 27, no. 11, pp. 1517–1524, Nov. 2020, doi: 10.1007/s12613-020-2001-8.

[14] J. J. Jeon, S. Mironov, Y. S. Sato, H. Kokawa, S. H. C. Park, and S. Hirano, "Grain Structure Development During Friction Stir Welding of Single-Crystal Austenitic Stainless Steel," *Metall. Mater. Trans. A*, vol. 44, no. 7, pp. 3157–3166, Jul. 2013, doi: 10.1007/s11661-013-1692-0.

[15] O. M. Barabash, R. I. Barabash, G. E. Ice, Z. Feng, and D. Gandy, "X-ray microdiffraction and EBSD study of FSP induced structural/phase transitions in a Ni-based superalloy," *Mater. Sci. Eng. A*, vol. 524, no. 1–2, pp. 10–19, Oct. 2009, doi: 10.1016/j.msea.2009.03.086.

[16] G. P. Dinda and A. Ramakrishnan, "Friction stir welding of high-strength steel," *Int. J. Adv. Manuf. Technol.*, vol. 103, no. 9–12, pp. 4763–4769, Aug. 2019, doi: 10.1007/s00170-019-04003-7.

[17] R. Ramesh, I. Dinaharan, R. Kumar, and E. T. Akinlabi, "Microstructure and Mechanical Characterization of Friction-Stir-Welded 316L Austenitic Stainless Steels," *J. Mater. Eng. Perform.*, vol. 28, no. 1, pp. 498–511, Jan. 2019, doi: 10.1007/s11665-018-3802-z.

[18] S. Shashi Kumar, N. Murugan, and K. K. Ramachandran, "Effect of friction stir welding on mechanical and microstructural properties of AISI 316L stainless steel butt joints," *Weld. World*, vol. 63, no. 1, pp. 137–150, Jan. 2019, doi: 10.1007/s40194-018-0621-7.

[19] W. C. Oliver and G. M. Pharr, “An improved technique for determining hardness and elastic modulus using load and displacement sensing indentation experiments,” *J. Mater. Res.*, vol. 7, no. 06, pp. 1564–1583, 1992.
[20] Q. Ma and D. R. Clarke, “Size dependent hardness of silver single crystals,” *J. Mater. Res.*, vol. 10, no. 4, pp. 853–863, Apr. 1995, doi: 10.1557/JMR.1995.0853.
[21] G. Farges and D. Degout, “Interpretation of the indentation size effect in vickers microhardness measurements-absolute hardness of materials,” *Thin Solid Films*, vol. 181, no. 1, pp. 365–374, 1989.
[22] W. D. Nix and H. Gao, “Indentation size effect in crystalline materials: A law for strain gradient plasticity,” *J. Mech. Phys. Solids*, vol. 46, no. 3, pp. 411–425, 1998.
[23] M. Shell De Guzman, G. Neubauer, P. Flinn, and W. D. Nix, “The Role of Indentation Depth on the Measured Hardness of Materials,” *MRS Proc.*, vol. 308, p. 613, 1993, doi: 10.1557/PROC-308-613.
[24] M. R. Maughan, A. A. Leonard, D. D. Stauffer, and D. F. Bahr, “The effects of intrinsic properties and defect structures on the indentation size effect in metals,” *Philos. Mag.*, vol. 97, no. 22, pp. 1902–1920, Aug. 2017, doi: 10.1080/14786435.2017.1322725.
[25] C. Tromas, “Hardness and elastic modulus gradients in plasma-nitrided 316L polycrystalline stainless steel investigated by nanoindentation tomography,” *Acta Mater.*, p. 9, 2012.
[26] K. S. Mao *et al.*, “Grain orientation dependence of nanoindentation and deformation-induced martensitic phase transformation in neutron irradiated AISI 304L stainless steel,” *Materialia*, vol. 5, p. 100208, Mar. 2019, doi: 10.1016/j.mtla.2019.100208.
[27] J. J. Roa, G. Fargas, A. Mateo, and E. Jiménez-Piqué, “Dependence of nanoindentation hardness with crystallographic orientation of austenite grains in metastable stainless steels,” *Mater. Sci. Eng. A*, vol. 645, pp. 188–195, Oct. 2015, doi: 10.1016/j.msea.2015.07.096.
[28] M. Haghshenas, M. A. Gharghouri, V. Bhakhri, R. J. Klassen, and A. P. Gerlich, “Assessing residual stresses in friction stir welding: neutron diffraction and nanoindentation methods,” *Int. J. Adv. Manuf. Technol.*, vol. 93, no. 9–12, pp. 3733–3747, Dec. 2017, doi: 10.1007/s00170-017-0759-2.
[29] Thomas H. Courtney, *Mechanical Behaviour of Materials*, 2nd ed. Waveland Press, Inc.
[30] S. Sabooni, F. Karimzadeh, M. H. Enayati, A. H. W. Ngan, and H. Jabbari, “Gas tungsten arc welding and friction stir welding of ultrafine grained AISI 304L stainless steel: Microstructural and mechanical behavior characterization,” *Mater. Charact.*, vol. 109, pp. 138–151, Nov. 2015, doi: 10.1016/j.matchar.2015.08.009.
[31] F. Legendre, S. Poissonnet, P. Bonnaillie, L. Boulanger, and L. Forest, “Some microstructural characterisations in a friction stir welded oxide dispersion strengthened ferritic steel alloy,” *J. Nucl. Mater.*, vol. 386–388, pp. 537–539, Apr. 2009, doi: 10.1016/j.jnucmat.2008.12.170.
[32] U. M. Chaudry, S.-C. Han, F. Alkelae, and T.-S. Jun, “Effect of PWHT on the Microstructure and Mechanical Properties of Friction Stir Welded DP780 Steel,” *Metals*, vol. 11, no. 7, p. 1097, Jul. 2021, doi: 10.3390/met11071097.
[33] C. A. Charitidis and D. A. Dragatogiannis, “Finite element analysis, stress-strain distribution and size effects rise during nanoindentation of welded aluminum alloy,” *Int. J. Struct. Integr.*, vol. 4, no. 1, pp. 78–90, Mar. 2013, doi: 10.1108/17579861311303645.
[34] Firouz Fadaeifard, M. R. Pakmanesh, M. S. Esfahani, K. A. Matori, and D. Chicot, “Nanoindentation Analysis of Friction Stir Welded 6061-T6 Al Alloy in As-Weld and Post Weld Heat Treatment,” *Phys. Met. Metallogr.*, vol. 120, no. 5, pp. 483–491, May 2019, doi: 10.1134/S0031918X1905003X.
[35] ASTM E112-13, “Standard Test Methods for Determining Average Grain Size,” ASTM International, West Conshohocken, PA, 2013. doi: 10.1520/E0112-13.
[36] D. J. Morris and Bahr, David F., “Nanoindentation: Localized Probes of Mechanical Behavior of Materials,” in *Springer Handbook of Experimental Solid Mechanics*, Springer, 2008, pp. 389–408. Accessed: Apr. 15, 2014. [Online]. Available: http://link.springer.com/10.1007/978-0-387-30877-7_16

[37] A. C. Fischer-Cripps, *Nanoindentation*. New York, NY: Springer New York, 2011. doi: 10.1007/978-1-4419-9872-9.

[38] T. Chen, L. Tan, Z. Lu, and H. Xu, “The effect of grain orientation on nanoindentation behavior of model austenitic alloy Fe-20Cr-25Ni,” *Acta Mater.*, vol. 138, pp. 83–91, Oct. 2017, doi: 10.1016/j.actamat.2017.07.028.

[39] A. L. Biro, B. F. Chenelle, and D. A. Lados, “Processing, Microstructure, and Residual Stress Effects on Strength and Fatigue Crack Growth Properties in Friction Stir Welding: A Review,” *Metall. Mater. Trans. B*, vol. 43, no. 6, pp. 1622–1637, Dec. 2012, doi: 10.1007/s11663-012-9716-5.

[40] N. Dialami, M. Chiumenti, M. Cervera, C. Agelet de Saracibar, and J. P. Ponthot, “Material flow visualization in Friction Stir Welding via particle tracing,” *Int. J. Mater. Form.*, vol. 8, no. 2, pp. 167–181, Apr. 2015, doi: 10.1007/s12289-013-1157-4.

[41] K. Kumar and S. V. Kailas, “The role of friction stir welding tool on material flow and weld formation,” *Mater. Sci. Eng. A*, vol. 485, no. 1–2, pp. 367–374, Jun. 2008, doi: 10.1016/j.msea.2007.08.013.

[42] M. Matsushita, Y. Kitani, R. Ikeda, M. Ono, H. Fujii, and Y. -D. Chung, “Development of friction stir welding of high strength steel sheet,” *Sci. Technol. Weld. Join.*, vol. 16, no. 2, pp. 181–187, Feb. 2011, doi: 10.1179/1362171810Y.0000000026.

[43] D. F. Bahr and W. W. Gerberich, “Plastic zone and pileup around large indentations,” *Metall. Mater. Trans. A*, vol. 27, no. 12, pp. 3793–3800, 1996.